

*Annual Review of Nuclear and Particle Science*  
**Probing the Neutrino-Mass  
 Scale with the KATRIN  
 Experiment**

Alexey Lokhov,<sup>1,2</sup> Susanne Mertens,<sup>3,4</sup> Diana S. Parno,<sup>5</sup>  
 Magnus Schlösser,<sup>6</sup> and Kathrin Valerius<sup>6</sup>

<sup>1</sup>Institute of Experimental Particle Physics, Karlsruhe Institute of Technology, Karlsruhe, Germany

<sup>2</sup>Institut für Kernphysik, Westfälische Wilhelms-Universität Münster, Münster, Germany

<sup>3</sup>Physik-Department, Technische Universität München, Garching, Germany; email: susanne.mertens@tum.de

<sup>4</sup>Max-Planck-Institut für Physik, München, Germany

<sup>5</sup>Department of Physics, Carnegie Mellon University, Pittsburgh, Pennsylvania, USA

<sup>6</sup>Institute for Astroparticle Physics, Karlsruhe Institute of Technology, Karlsruhe, Germany; email: kathrin.valerius@kit.edu

ANNUAL  
REVIEWS **CONNECT**

[www.annualreviews.org](http://www.annualreviews.org)

- Download figures
- Navigate cited references
- Keyword search
- Explore related articles
- Share via email or social media

Annu. Rev. Nucl. Part. Sci. 2022. 72:259–82

First published as a Review in Advance on  
 July 8, 2022

The *Annual Review of Nuclear and Particle Science*  
 is online at [nucl.annualreviews.org](http://nucl.annualreviews.org)

<https://doi.org/10.1146/annurev-nucl-101920-113013>

Copyright © 2022 by Annual Reviews. This work is licensed under a Creative Commons Attribution 4.0 International License, which permits unrestricted use, distribution, and reproduction in any medium, provided the original author and source are credited. See credit lines of images or other third-party material in this article for license information.



## Keywords

neutrino mass, direct kinematic method, tritium beta decay

## Abstract

The absolute mass scale of neutrinos is an intriguing open question in contemporary physics. The as-yet-unknown mass of the lightest and, at the same time, most abundant massive elementary particle species bears fundamental relevance to theoretical particle physics, astrophysics, and cosmology. The most model-independent experimental approach consists of precision measurements of the kinematics of weak decays, notably tritium  $\beta$  decay. With the KATRIN experiment, this direct neutrino-mass measurement has entered the sub-eV domain, recently pushing the upper limit on the electron-based neutrino mass down to 0.8 eV (90% CL) on the basis of first-year data out of ongoing, multiyear operations. Here, we review the experimental apparatus of KATRIN, the progress of data taking, and initial results. While KATRIN is heading toward the target sensitivity of 0.2 eV, other scientific goals are pursued. We discuss the search for light sterile neutrinos and an outlook on future keV-scale sterile-neutrino searches as well as further physics opportunities beyond the Standard Model.

## Contents

1. INTRODUCTION .....	260
2. THE KATRIN EXPERIMENT .....	263
2.1. Working Principle and Experimental Setup .....	263
2.2. Commissioning Results .....	265
2.3. Systematic Effects and Calibration Measurements .....	266
3. STATUS OF DATA TAKING AND CURRENT RESULTS .....	268
3.1. Constructing the Experimental $\beta$ -Decay Spectrum .....	268
3.2. $\beta$ -Spectrum Model and Analysis Tools .....	269
3.3. Early Neutrino-Mass Results .....	271
3.4. Sterile-Neutrino Results .....	274
4. THE FUTURE OF KATRIN .....	275
4.1. Outlook on Long-Term Data Taking and Projected Sensitivity .....	275
4.2. Beyond-Standard-Model Physics in Precision $\beta$ -Decay Spectroscopy .....	277
5. SUMMARY .....	278

## 1. INTRODUCTION

In the original formulation of the Standard Model, neutrinos appear as massless fermions. The discovery of neutrino oscillation (1, 2) established that neutrinos have three distinct mass states ( $\nu_1, \nu_2, \nu_3$ ), which are quantum superpositions of the electron, muon, and tau flavor states ( $\nu_e, \nu_\mu, \nu_\tau$ ). The mixing of the flavor states  $\alpha$  with the mass states  $i$  is given by the elements  $U_{\alpha i}$  of the Pontecorvo-Maki-Nakagawa-Sakata (PMNS) matrix. Neutrino flavor oscillation arises from the dependence of the propagation Hamiltonian on the neutrino-mass values and requires a finite splitting between the  $\nu_i$  mass states.

The existence of neutrino oscillations, and therefore of nonzero neutrino mass, is the first laboratory evidence of physics beyond the Standard Model. Neutrinos are at least five orders of magnitude less massive than electrons, the next lightest fermions. Finite neutrino mass cannot be naturally explained by the Higgs field; in fact, the underlying dynamical mechanism is unknown. The absolute neutrino-mass scale—or, equivalently, the mass of the lightest neutrino state—is therefore a crucial input to particle theory.

Neutrino-oscillation experiments can probe the PMNS-matrix elements, the mass splittings, and the mass ordering [i.e., whether  $m_1 < m_2 < m_3$  (normal) or  $m_3 < m_1 < m_2$  (inverted)]; however, they have no sensitivity to the mass scale. In principle, four complementary approaches rooted in cosmology, astrophysics, and particle and nuclear physics provide experimental and observational access to this quantity. A comprehensive picture can be found, e.g., in the recent review in Reference 3; here, we give a brief summary.

Neutrinos were copiously produced in the early universe. Despite having small individual masses, these relic neutrinos collectively had a significant impact on the formation of large-scale cosmological structures. Within the context of the  $\Lambda$  cold-dark-matter ( $\Lambda$ CDM) model, the Dark Energy Survey recently inferred an upper limit of  $\Sigma m_i < 0.13$  eV [95% confidence level (CL)] by combining their own galaxy-clustering and gravitational-lensing data with data sets from the Planck cosmic-microwave-background measurement, baryon-acoustic oscillations, Type Ia supernovae, and redshift-space distortions (4). This constraint is strongly dependent on the specific cosmological model used (i.e.,  $\Lambda$ CDM concordance); when interpreted in the  $w$  cold-dark-matter

model, for example, the same data sets yield a relaxed constraint of  $\Sigma m_i < 0.17$  eV (95% CL) (4). (Throughout this article, we use natural units, in which  $c = \hbar = 1$ .)

In astrophysics, the neutrino mass may also be probed via dispersion in supernova-neutrino time-of-flight data. The timing distribution of SN1987A neutrinos yields an upper limit of  $m_\nu^{\text{TOF}} < 5.7$  eV (95% CL) (5), effectively applicable to all mass states; further improvements must await the next galactic supernova.

If neutrinoless double-beta decay ( $0\nu\beta\beta$ ; recently reviewed in Reference 6) occurs and is driven predominantly by light-neutrino exchange, the  $0\nu\beta\beta$  rate will depend on the effective neutrino mass  $\langle m_{\beta\beta} \rangle = |\sum U_{ei}^2 m_i|$ . To date, the most sensitive limits on  $\langle m_{\beta\beta} \rangle$  are set at 90% CL by searches in  $^{76}\text{Ge}$  (GERDA, 0.08–0.18 eV) (7) and in  $^{136}\text{Xe}$  (KamLAND-Zen, 0.06–0.17 eV) (8); in both cases, uncertainties in nuclear-matrix elements account for the ranges of the limits. Of course, these limits are valid only if neutrinos are Majorana fermions; if they are Dirac fermions, the  $0\nu\beta\beta$  rate vanishes and so does the mass sensitivity.

Direct kinematic measurements of the endpoint region of the spectrum from  $\beta$  decay or electron capture probe the incoherent sum of the neutrino masses

$$m_\nu^2 = \sum_i |U_{ei}|^2 m_i^2 = m_\beta^2. \quad 1.$$

Here we denote the observable  $m_\nu$ ; it is often given as  $m_\beta$  in the literature (3). This laboratory-based approach is independent of the neutrino nature (Dirac or Majorana) and of the underlying cosmological models, depending only on the reconstruction of the decay kinematics. Precision experiments need to understand the propagation and energy losses of decay products within the experiment. A degree of theoretical dependence arises via the necessary calculation of atomic and molecular states of the mother and daughter nuclei (9, 10). **Figure 1** shows the relationships between  $\Sigma m_i$ ,  $\langle m_{\beta\beta} \rangle$ , and  $m_\nu$ .

In principle, many  $\beta$ -decay and electron-capture isotopes are possible candidates. Currently, tritium and holmium-163 have been established as the isotopes of choice due to their low  $Q$  value

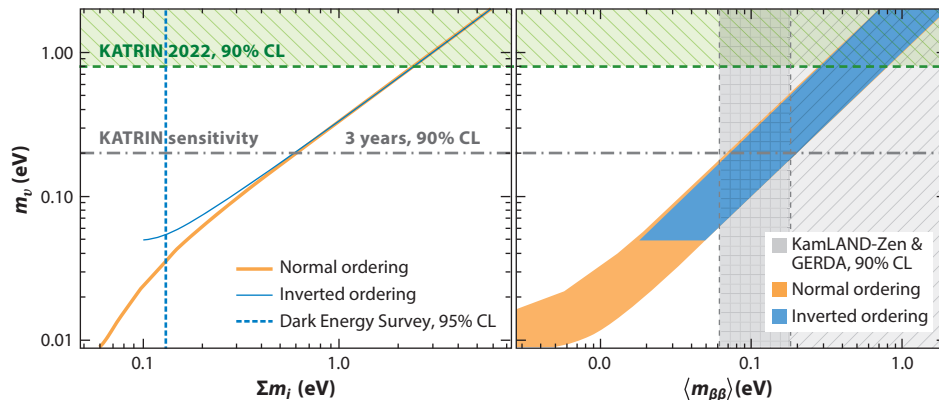
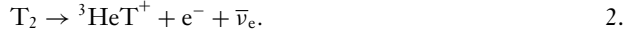


**Figure 1**

Complementary neutrino-mass observables. (*Left*) Incoherent sum of neutrino masses  $m_\nu$  for different  $\Sigma m_i$ , based on recent oscillation data for normal (*orange*) and inverted (*blue*) mass ordering (11). (*Right*) Allowed ranges for  $\langle m_{\beta\beta} \rangle$  and  $m_\nu$ . In both panels, the horizontal dashed green line shows the upper limit obtained by KATRIN, and the dash-dotted gray line shows the design sensitivity of KATRIN after 3 net years of measurement time. The vertical lines show the most stringent upper limits from the Dark Energy Survey (4) (*left panel; dashed blue*) and from the KamLAND-Zen (8) and GERDA (7) experiments (*right panel; gray dashed lines*) indicate the range of the upper limits on  $\langle m_{\beta\beta} \rangle$ .

[ $Q(T) = 18.575$  keV,  $Q_{\text{EC}}(^{163}\text{Ho}) = 2.833$  keV] and thus favorable phase space and also due to the availability of a suitable amount of nuclear material. Both isotopes have short half-lives compared to other low- $Q$  decays [ $t_{1/2}(T) = 12.3$  years,  $t_{1/2}(^{163}\text{Ho}) = 4,570$  years], and thus offer high accessible activity. Even though the experimental realizations are rather different, both approaches search for a distortion of the energy spectrum near the kinematic endpoint induced by the tiny neutrino rest mass.

Although atomic tritium,  $T$ , would be the simpler system, all recent  $\beta$ -decay experiments have employed the molecular form,  $T_2$ . The decay scheme is



The decay energy becomes the kinetic energy and rest mass of the decay products. Furthermore, the molecular ion,  ${}^3\text{HeT}^+$ , will be produced with probability  $\zeta_f$  in a state of excitation energy  $V_f$ , both of which can be calculated by quantum-chemical methods incorporating rotational, vibrational, and electronic excitations (12). For the  $\beta$  decay of molecular tritium, the differential spectrum for  $\beta$  electrons ( $m_e$ ) with kinetic energy  $E$  is given by

$$R_\beta(E) = \frac{G_F^2 \cos^2 \Theta_C}{2\pi^3} |M_{\text{nuc}}|^2 F(E, Z' = 2) \cdot (E + m_e) \sqrt{(E + m_e)^2 - m_e^2} \cdot \sum_f \zeta_f \varepsilon_f(E) \sqrt{\varepsilon_f(E)^2 - m_\nu^2} \Theta[\varepsilon_f(E) - m_\nu]. \quad 3.$$

The energy-independent prefactors include the Fermi constant  $G_F$ , the Cabibbo angle  $\Theta_C$ , and the nuclear-matrix element  $|M_{\text{nuc}}|^2$ .  $F(E, Z' = 2)$  is the Fermi function. Here,  $\varepsilon_f(E) = E_0 - V_f - E$ , where  $E_0$  denotes the maximum kinetic energy of the electron, in the case of zero neutrino mass. A derivation is found in Reference 13. The shape imprint of the neutrino mass relates to the squared value  $m_\nu^2$ , which is the extracted fit parameter in the analysis.

Over the past three decades, tritium-based neutrino-mass searches have made substantial advances in terms of both instrumentation and the theoretical description of the  $\beta$ -decay spectrum. On the theory side, developments notably include the advent of precision quantum-chemical computations of electronic and molecular excitations in the final product of tritium  $\beta$  decay (12; see also Reference 9 for an overview). A major improvement on the instrumentation side was the replacement of magnetic spectrometers with electrostatic filters with magnetic adiabatic collimation (MAC-E filters), developed for neutrino-mass measurements by groups at Mainz and Troitsk (14, 15); see Section 2. The combination of an electrostatic retardation filter with a magnetic bottle for momentum collimation allows for both excellent energy resolution and large angular acceptance. The Mainz group used a quench-condensed tritium source on a cold substrate in combination with a MAC-E filter, whereas the Troitsk group applied the same spectroscopic technique to electrons emitted from a gaseous  $T_2$  source refined from that developed for the LANL experiment (16). Both the Mainz and Troitsk groups eventually reported very similar final upper limits on the effective electron neutrino mass,  $m_\nu < 2.3$  eV (95% CL) (17) and  $m_\nu < 2.05$  eV (95% CL) (18), respectively. New technologies, such as cyclotron radiation emission spectroscopy and atomic tritium sources pursued by the Project 8 collaboration, may eventually extend the sensitivity of tritium-based neutrino-mass experiments below 0.2 eV (19, 20).

An electron-capture spectrum differs from Equation 3 due to the Breit-Wigner shapes associated with capture of electrons from different atomic shells, but the phase-space term describing the  $m_\nu^2$  dependence is identical. In the holmium-based measurement, first proposed in Reference 21, the  $^{163}\text{Ho}$  atom decays into  $^{163}\text{Dy}^*$  and an electron neutrino, after which the  $^{163}\text{Dy}^*$  releases its excitation energy via various atomic transitions. By embedding the source material into a microcalorimeter, the differential energy spectrum can be measured with high resolution to search

for the signature of the neutrino rest mass. Two collaborations are following different strategies for sub-eV  $m_\nu$  sensitivity. ECHO (22) employs metallic magnetic calorimeters (23, 24) with a targeted activity of 10 Bq per detector, and HOLMES (25) uses transition-edge sensors (26) with each detector loaded with an activity of 300 Bq, leading to different pileup fractions and total numbers of detectors. In 2019, ECHO reported an upper limit of  $m_\nu < 150$  eV (95% CL) from a 16-pixel detector array (27).

In this article, we review the status and prospects of the Karlsruhe Tritium Neutrino (KATRIN) experiment, which has set world-leading limits on the neutrino-mass scale via direct measurement of the endpoint region of the tritium  $\beta$  spectrum (28, 29). Section 2 explains KATRIN's objectives, working principle, commissioning history, and systematics studies. Section 3 details the construction of both experimental and model spectra; the analysis methods for comparing the two; neutrino-mass results; and results of searches for additional, sterile-neutrino flavors that do not interact via the weak force. Finally, in Section 4 we give a brief perspective on KATRIN's long-term outlook.

## 2. THE KATRIN EXPERIMENT

The KATRIN experiment was conceived to develop the successful MAC-E-filter technique well into the sub-eV domain (30). Notably, the experimental observable in a kinematic neutrino-mass search is the squared neutrino mass,  $m_\nu^2$  (Equation 3). Hence, the goal of pushing the sensitivity on the absolute mass scale,  $m_\nu$ , by a factor of ten from 2 to 0.2 eV (90% CL) requires an improvement by a factor of 100 in systematic as well as statistical uncertainties. The target sensitivity of KATRIN is based on a total systematic uncertainty of  $\sigma_{\text{sys,tot}}(m_\nu^2) = 0.017$  eV<sup>2</sup>, to be closely matched by an expected statistical uncertainty of  $\sigma_{\text{stat}}(m_\nu^2) = 0.018$  eV<sup>2</sup> after approximately 3 net years of beam time.

Achieving this goal requires solutions to numerous technological challenges in constructing, understanding, and operating the experiment. A detailed technical description of the apparatus, as well as the commissioning results, is given in Reference 31 and further references therein. For this review, we focus on the working principle of KATRIN and outline the key functions of its beamline components (Section 2.1) before briefly summarizing commissioning (Section 2.2) and systematics (Section 2.3).

### 2.1. Working Principle and Experimental Setup

The KATRIN beamline, depicted in **Figure 2**, is 70 m long. The size and complexity of the experimental apparatus are driven by the challenges of providing an ultrahigh-intensity source of tritium  $\beta$ -decay electrons with high stability, performing a precision shape measurement of the  $\beta$  spectrum close to the kinematic endpoint at 18.6 keV, and achieving a low rate of background events.

**2.1.1. Source and transport section.** Three of KATRIN's six major subsystems are housed inside the Tritium Laboratory Karlsruhe, forming the source and transport section of the experiment. The cryostat of the windowless gaseous tritium source comprises a 10-m-long, 90-mm-diameter beam tube that is kept in a strong magnetic field by a chain of superconducting solenoids. T<sub>2</sub> gas is injected at the midpoint of the beam tube and is continuously pumped out at both ends. The source tube can be cooled to 30 K to reduce thermal motion of the molecules. The tritium is circulated in a closed-loop system, in which exhaust gas from the decay volume is purified to reach a tritium fraction of well above 95% and is subsequently reinjected into the beam tube. This way, a cumulative 40 g of tritium is processed in the closed-loop system per day. The instantaneous

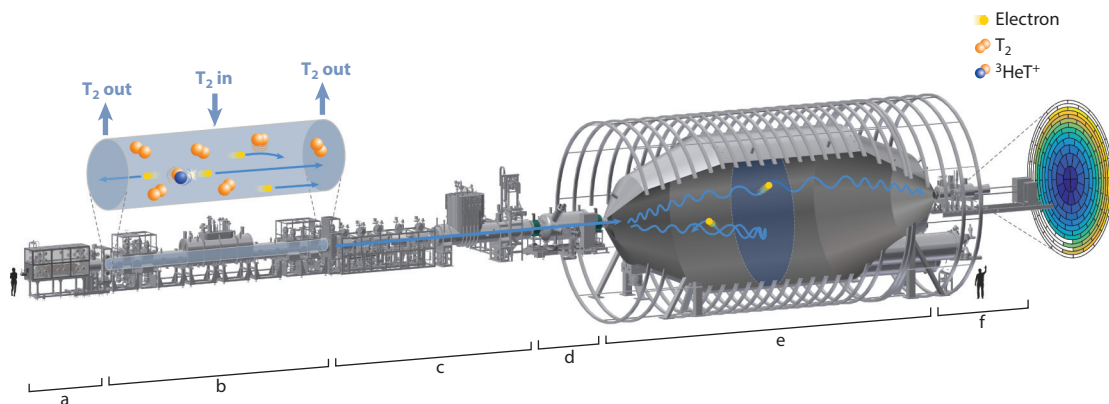


**Figure 2**

Overview of the KATRIN beamline, detailing its main components: (a) rear calibration and monitoring system, (b) windowless gaseous tritium source, (c) differential and cryogenic pumping sections, (d) prespectrometer, (e) main-spectrometer vessel enclosed in air coils, and (f) focal-plane detector system. An enlarged view of the segmented detector wafer is projected to the right. Figure adapted from Reference 29 (CC BY 4.0).

tritium content of the source, approximately 30  $\mu\text{g}$ , generates up to  $10^{11}$   $\beta$ -decay electrons per second; these electrons follow the magnetic-field lines of the solenoid fields in both upstream and downstream directions. At a nominal value of  $5 \times 10^{17}$  molecules/ $\text{cm}^2$ , the stationary-state tritium column density is optimized to yield maximum luminosity while limiting electron scattering in the gas to a moderate level. The tritium concentration is continuously measured by an external laser Raman system (32).

In the transport section downstream of the source cryostat, a combination of turbomolecular pumps and a cold trap at a temperature of 3 to 4 K reduces the flow of tritium molecules by at least 12 orders of magnitude, as  $\beta$  electrons are transported along magnetic-field lines toward the spectrometers.

Upstream of the source, a calibration and monitoring system ensures that source properties can be stabilized as well as monitored (see Section 2.3). It houses a gold-plated disc (dubbed the rear wall), which provides a controlled electric bias potential at the upstream end of the source tube. Electrons from a precision photoelectron source (electron gun) with adjustable beam energy can be injected into the beamline for calibration purposes. Two systems monitor tritium activity: a  $\beta$ -induced X-ray spectroscopy system (33) at the rear end of the source and a silicon-diode system downstream, directly adjacent to the spectrometer section, for electron counting at the edge of the electron beam (34).

Monoenergetic conversion electrons from  $^{83\text{m}}\text{Kr}$  (35) can be delivered by a condensed krypton source at the exit of the transport section or generated directly inside the source beam tube through cocirculation of gaseous krypton with the tritium. These calibration modes probe different systematic uncertainties ranging from work-function changes to local electric potentials in the source plasma.

**2.1.2. Spectrometer and detector section.** Downstream of the tritium-related systems are the prespectrometer and main spectrometer, both large-volume MAC-E filters, as well as the focal-plane electron detector. At 23 m length and 10 m diameter, the main-spectrometer vessel operates at a residual gas pressure of  $10^{-11}$  mbar to ensure minimum energy loss inside the MAC-E

filter. This ultrahigh vacuum level is maintained by turbomolecular pumps and a large-area getter pump, with a total pumping speed for hydrogen of  $2.5 \times 10^5$  L/s. To improve vacuum conditions, the stainless-steel vessel can be baked out at temperatures up to 200°C. The vessel serves as a high-voltage electrode, lined with a two-layer, modular inner electrode system that fine-tunes the electric field and provides electrostatic shielding against external background. An electron entering the spectrometer through the grounded beam tube from the source will thus feel an increasingly strong electrostatic retarding potential that reaches its maximum at the central, analyzing plane of the vessel. From the continuous  $\beta$  spectrum, only those electrons with sufficient kinetic energy will be able to pass this longitudinal electrostatic barrier; all other electrons will be electrostatically reflected. An integrated spectrum (as for a high-pass filter) can thus be recorded by stepping through a range of values of the retarding potential. This is the first ingredient of the MAC-E-filter principle.

The second ingredient is formed by the magnetic field and its gradient. The magnetic field inside the spectrometer is produced mainly by the entrance and exit superconducting solenoids, and its fine-tuning is achieved by two large sets of air-cooled magnet coils surrounding the spectrometer vessel, in axial and radial configuration. This system also allows for correction for the Earth's magnetic field, which would otherwise lead to a significant distortion of the magnetic flux tube. Between the entrance (exit) solenoid and the central plane of the spectrometer, the magnetic field strength drops adiabatically by approximately four orders of magnitude from  $B_{\text{src}} = 2.52$  T ( $B_{\text{max}} = 4.24$  T) to  $B_{\text{min}} = 6.3 \times 10^{-4}$  T. This inverse magnetic-bottle effect causes a magnetic gradient force to act on an electron entering the spectrometer from the strong magnetic field inside the tritium source and transport section. As the electron travels toward the center of the spectrometer, its perpendicular momentum  $p_{\perp}$  (sustaining the cyclotron motion) will be transformed into longitudinal momentum  $p_{\parallel}$  (parallel to the magnetic-field line), according to the conservation of the angular magnetic moment,  $\mu = E_{\perp}/B = \text{constant}$  in the nonrelativistic approximation. Thus, the energy due to cyclotron motion,  $E_{\perp}$ , will be reduced along the electron trajectory as the electron passes from a strong magnetic field into a weaker one. The reverse effect takes place as a transmitted electron leaves the analyzing plane behind and is reaccelerated to its original kinetic energy in the downstream direction. This adiabatic magnetic collimation (and subsequent decollimation) of the electron momentum allows the MAC-E filter to reach an energy resolution (or, more precisely, filter width)  $\Delta E$ , which scales directly with the ratio of minimum to maximum magnetic field along the trajectory. This method requires large spectrometer dimensions: The inner diameter is determined by the conservation of the transported magnetic flux. The magnetic-field settings chosen for the first KATRIN neutrino-mass runs result in a filter width of  $E_0 \cdot B_{\text{min}}/B_{\text{max}} \approx 2.8$  eV, where  $E_0 = 18.6$  keV.

The focal-plane detector, situated at the downstream end of the beamline, counts the electrons passing the MAC-E filter for each given set point of the retarding potential during a given time interval. The detector consists of a silicon *p-i-n* diode, segmented into 148 pixels of equal area in a dartboard pattern. Radial and azimuthal segmentation permits accounting for a radial-dependent background rate, spatial nonuniformity of transmission properties, and potential radial-dependent effects of the tritium source. The detector is placed inside a strong magnetic field to focus the flux of electrons onto the sensitive area, 90 mm in diameter. The detector system also includes a muon veto, a postacceleration electrode, and instrumentation for regular calibration.

## 2.2. Commissioning Results

KATRIN commissioned individual subsystems and groups of subsystems before beginning to commission the entire beamline (36). For subsystem commissioning work, we highlight several

studies of the large-volume spectrometers: the vacuum performance (37), different background processes and their mitigation (38–41), and electromagnetic properties (42). Upstream, we note demonstrations of the control and monitoring systems for the tritium source (43) and of the temperature stability of the source beam tube (44, 45).

The beamline was completed in 2016 and was commissioned with photoelectrons created by illumination of the gold-plated rear wall with ultraviolet light (46). The following year, the introduction of short-lived  $^{83\text{m}}\text{Kr}$  ( $t_{1/2} = 1.8$  h) provided an isotropic commissioning source for more detailed probes of the system response function (Section 3.2). With the KATRIN main spectrometer, the line widths of the narrow K-32 and L<sub>3</sub>-32 conversion electrons were measured with percent-level precision (47). Furthermore, the measured line splittings allowed for a stability assessment of the retarding potential (Section 2) (48, 49).

The tritium circulation loop system was connected to the KATRIN source for the first time in spring 2018 and was commissioned with deuterium gas before tritium commissioning in May–June 2018 (50). Very low tritium activity was achieved by mixing pure deuterium with approximately 0.5% tritium, producing a gas in radiochemical equilibrium at approximately 99% D<sub>2</sub> and 1% DT. The overall  $\beta$ -decay activity was demonstrated to be stable at the 0.1% level (50).

Safe operation requires tritium retention in the source and transport section, thereby preventing contamination of the spectrometers. The retention of neutral gas via differential and cryo-pumping had already been demonstrated in test experiments with deuterium (51). However, tritium could in principle enter into the spectrometers in ionic forms (e.g., T<sup>+</sup> or T<sub>3</sub><sup>+</sup>) generated via  $\beta$  decay or via ionization of T<sub>2</sub> gas by  $\beta$  electrons. As these species are not pumped but follow magnetic-field lines from source to spectrometer, a system of blocking and drifting electrodes is required (52) and exceeds specifications (53).

Out of 116  $\beta$  spectra recorded during the first tritium campaign, 82 passed quality cuts and were used to successfully test different techniques for combining spectra from individual scans and individual pixels to obtain representative fit results. In addition, two methods for addressing systematic uncertainties were successfully implemented and tested. Excellent agreement of the spectrum calculation with the data was achieved (50). The effective endpoint  $E_0$  was determined with 250-meV precision and was shown to be stable over the entire campaign.

After this initial demonstration of tritium running, but before the first neutrino-mass campaign, KATRIN commissioned the electron-gun system and then used it to measure the energy-loss function using a special time-of-flight spectrometer mode (Section 2.3). Further systematics, such as the spatial inhomogeneity of the work function of the rear wall, were investigated (53). During the ramp-up of tritium activity in preparation for the first neutrino-mass campaign, KATRIN completed qualification of the ion-blocking instrumentation (54, 55) and measured the energy-loss function at several column densities (56).

The experiment has finally reached a phase of steady-state neutrino-mass data taking, with an expected total duration of 1,000 days, not counting scheduled maintenance (Section 4.1).

### 2.3. Systematic Effects and Calibration Measurements

To determine the neutrino mass from the measured  $\beta$  spectrum, the experimental and theoretical input parameters for the analytical spectral description (Section 3.2) must be known with high accuracy. Any uncertainty in these parameters or gap in the model will propagate into the systematic uncertainty of the observable  $m_\nu^2$ . The systematic effects can be separated into signal-related and background-related categories.

**2.3.1. Signal-related systematic effects.** The shape of the transmission function of the  $\beta$  electrons through the main spectrometer is determined by relevant magnetic fields: the source field

$B_{\text{src}} = 2.52$  T in which the  $\beta$  electron is created, the maximum beamline field  $B_{\text{max}} = 4.74$  T, and the low magnetic field in the analyzing plane of the main spectrometer  $B_{\text{ana}} = \mathcal{O}(10^{-4}$  T). The latter field cannot be measured directly in place. A net of precision magnetic-field sensors is therefore installed around the vacuum vessel (57) from which the magnetic field inside is inferred via simulations with the Kassiopeia framework (58); presently, the related uncertainty is on the 1% level. The strong fields  $B_{\text{src}}$  and  $B_{\text{max}}$  were characterized by field mapping with precision probes (59), and their stability can be monitored. The estimated uncertainties are  $\sigma(B_{\text{src}}) = 1.7\%$  and  $\sigma(B_{\text{max}}) = 0.1\%$ . Precision spectroscopy of  $^{83\text{m}}\text{Kr}$  lines validates the transmission model.

KATRIN must also understand how the  $\beta$  electrons lose energy on their way from the source to the detector. Crucially important is inelastic scattering with  $\text{T}_2$ , which depends on  $\rho d \sigma$ , the product of the tritium column density  $\rho d$  and the scattering cross section  $\sigma$ . This parameter is determined every few days by a calibration with the electron gun in the rear section, which provides a monoenergetic and stable electron beam. The ratio of scattered to unscattered electrons is then used to derive  $\rho d \sigma$ . In between these dedicated calibration measurements, the  $\rho d$  stability is continuously monitored via activity measurements (Section 2.1.1). In addition, the tritium activity is measured once per scan by the focal-plane detector at a retarding potential 300 V below the endpoint. By decoupling activity drifts from tritium concentration drifts as recorded by Raman spectroscopy (32), one can determine  $\rho d \sigma$  with less than 0.25% uncertainty.

The energy-loss function describes the probability that a  $\beta$  electron loses a certain amount of energy in an inelastic scattering with a  $\text{T}_2$  molecule. It is parameterized by nine empirically determined parameters derived from dedicated measurements with the electron gun (56). This systematic effect was considered especially challenging at the time of the 2004 technical design report (60), but today the related uncertainty is well below the required value.

Another key systematic effect for the signal electrons is the potential in which they are created by  $\beta$  decay in the source. Intense  $\beta$ -decay activity leads to secondary ionization of the source gas and thus to the generation of a cold magnetized plasma. The plasma potential is shaped by boundary conditions on the beam tube and on the rear wall that terminates the charge transport on the magnetic flux tube, as well as by the interaction of diffusing gas and ions. An unknown absolute source potential will be absorbed by the effective endpoint, which is a free parameter in the fit. Spatial inhomogeneities and temporal drifts of the overall potential, however, can lead to a broadening of the response function by  $\sigma_p^2$ . Furthermore, a longitudinal forward-backward asymmetry of the potential  $\Delta_p$  can be defined. This results in a shift of the energy spectrum associated with scattered electrons (originating mainly from the rear of the source) compared to the spectrum of the unscattered electrons (mainly from the front of the source). Both parameters can be probed using high-resolution spectroscopy of a  $^{83\text{m}}\text{Kr}$  calibration source cocirculating with  $\text{T}_2$ .

**2.3.2. Background-related systematic effects.** The design sensitivity of KATRIN requires a background rate of  $\mathcal{O}(10$  mcps). First measurements revealed a higher rate of the order of  $\mathcal{O}(1$  cps), and successful measures were taken to identify and mitigate several sources of background (38–41). Since the MAC-E filter decelerates signal  $\beta$  electrons nearly to rest, very low-energy secondary electrons created in the main-spectrometer volume cannot be distinguished from signal in the detector.

A major source of the residual background is related to  $^{219}\text{Rn}$  emanating from the nonevaporable getter pump material that maintains the main-spectrometer vacuum (61). Radon atoms propagate into the spectrometer volume and decay there, emitting electrons with energies in the range of 10–100 keV. These electrons are trapped magnetically between the superconducting solenoids at the entrance and the exit of the spectrometer and scatter on the residual gas in the volume of the spectrometer, producing secondary electrons that could eventually reach the

detector. The radon atoms are efficiently (up to 95%) retained by the liquid-nitrogen-cooled baffles installed in front of the getter pumps. The small remaining amount of radon is responsible for the non-Poisson component of the background rate, because—being produced by a single primary particle—the secondary electrons are correlated in time. The larger dispersion of the count-rate distribution effectively increases the statistical uncertainty assigned to each measurement point in the spectral fit and the uncertainty of the fit parameters.

The remaining major component of the background exhibits a clear volume dependency and is attributed to radioactivity in the walls of the spectrometer vessel (62). Within the wall, an  $\alpha$  decay with high recoil momentum could sputter atoms in highly excited (Rydberg) states from the walls. These atoms propagate into the volume, where they are distributed almost uniformly and can be ionized by thermal radiation, emitting low-energy background electrons.

Apart from increasing statistical uncertainties, background may influence the shape of the measured  $\beta$  spectrum. The background rate may have a small dependence on the absolute retarding potential applied to the spectrometer. To first order, this dependence can be modeled as a linear function of  $qU$ , which was studied in a dedicated measurement. The slope is introduced in the spectral fits as a constrained systematic parameter.

Another background is related to the Penning trap between the pre- and main spectrometers. To clear the trap, a special electron catcher can move into the flux tube and remove stored electrons in the middle of the trap (63). The movement is performed while changing the retarding potential during a scan. Between movements, the filling of the trap causes a small increase of the background count rate, of order 1  $\mu\text{cps/s}$ . The measurement time spent at each retarding potential is optimized for neutrino-mass sensitivity and varies significantly for different measurement points. Therefore, points with longer measurement times would have higher background rates by up to 1  $\text{mcp/s}$ , causing a shape distortion of the measured spectrum. This increase of the count rate is estimated from the study of the rate evolution within a measurement point and is included in the fitting as an additional systematic parameter. To mitigate this effect in later campaigns, the voltage of the prespectrometer was set to a lower value of  $-100$  V, removing the Penning trap entirely.

### 3. STATUS OF DATA TAKING AND CURRENT RESULTS

#### 3.1. Constructing the Experimental $\beta$ -Decay Spectrum

As seen in Section 2, KATRIN measures an integral spectrum, varying the integration threshold to map out the spectral shape. Each data-taking campaign consists of some number of spectral scans, and each scan is built up out of a predefined set of scan steps at a specific set point of the retarding potential  $U$  (thus defining the integration energy threshold  $qU$  for an electron of charge  $q$ ). The time spent at each scan step follows a predetermined measurement-time distribution (see **Figure 3c**). The scanned energy interval is chosen to be larger than the spectral-analysis interval, which allows for rate monitoring deeper in the spectrum. Each scan takes approximately 2.5 h; KATRIN alternates scans with increasing and decreasing  $qU$  to mitigate effects of drifts in various subsystems (64).

Electrons are counted in the segmented focal-plane detector (**Figure 2, right**). Each pixel triggers independently, and the energy and timing of each event are reconstructed online (65). Scans are selected for analysis on the basis of whether slow-controls parameters show stable, nominal operation. Any individual scan lacks the statistics to extract a neutrino mass from a spectral fit according to the methods described in Section 3.2. Instead, for a given measurement period, all scans that pass the slow-controls quality cuts are combined into a single spectrum, stacking scan steps with matching  $qU$  set points into bins. This method results in a small systematic uncertainty due to scan-to-scan fluctuations.

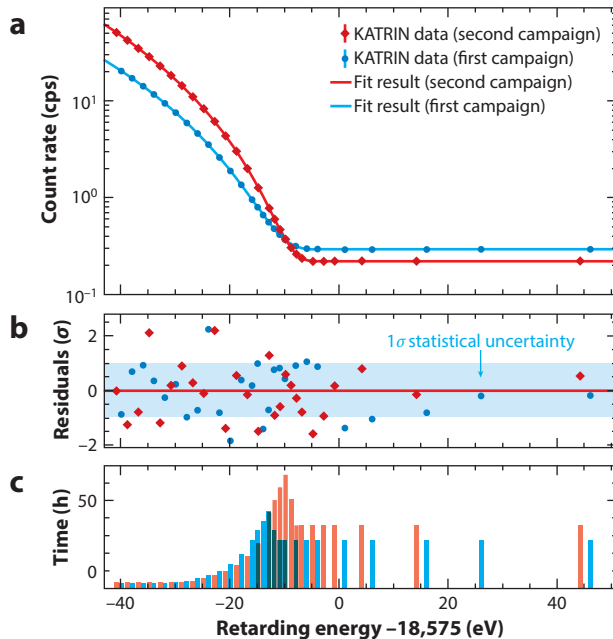


**Figure 3**

Tritium  $\beta$  spectra measured by KATRIN near the kinematic endpoint. (a) Measured rate at each retarding energy  $qU$  for the first (KNM1; blue) and second (KNM2; red) KATRIN measurement campaigns (29, 64). The lines depict a simultaneous fit to the data of both neutrino-mass campaigns. (b) Residuals for the combined fit. The blue band shows the  $1\sigma$  statistical uncertainty. (c) Total measurement times at each scan step in KNM1 and KNM2. The latter measurement-time distribution was adapted to take advantage of an improved signal-to-background ratio.

Meanwhile, it is computationally prohibitive to fit the spectrum for each pixel individually. Instead, pixels are typically combined into regions, wherein the spectra may be summed without severe systematics from variations across the analyzing plane. In the first measurement campaign (28, 64), all accepted pixels were combined into a single, uniform spectrum. In the second (29), the pixels were grouped into concentric annuli, either one pixel or three pixels wide, to account for hypothesized radial effects in the source. The analysis of later measurement campaigns must account for larger potential variations across the analyzing plane (Section 4.1). The pixels are therefore grouped into patches that deviate from the concentric rings but that exhibit similar analyzing-plane potentials as determined from commissioning data.

Operational parameters may vary significantly between measurement campaigns (see **Table 1**, below). For this reason, summing spectra from different measurement campaigns is typically inappropriate. Instead, KATRIN's overall data set may be treated by various statistical techniques, as summarized in Section 3.3 and Reference 29.

### 3.2. $\beta$ -Spectrum Model and Analysis Tools

The integral tritium  $\beta$  spectrum  $R(qU)$  measured by KATRIN is described by a convolution of the differential  $\beta$ -electron spectrum,  $R_\beta(E)$  (see Equation 3 and Reference 66), and the response function of the KATRIN setup  $f(E, qU)$ , to which a background rate  $R_{\text{bg}}$  is added:

$$R(qU) = A_s \cdot N_{T, \text{eff}} \int R_\beta(E) \cdot f(E, qU) dE + R_{\text{bg}}. \quad 4.$$

**Table 1** Key operational parameters for the first [KNM1 (28)] and second [KNM2 (29)] KATRIN neutrino-mass campaigns

	KNM1	KNM2
Number of scans	274	361
Total scan time	521.7 h	743.7 h
Background rate	290 mcps	220 mcps
$T_2$ column density	$1.11 \times 10^{17} \text{ cm}^2$	$4.23 \times 10^{17} \text{ cm}^2$
Source activity	$2.5 \times 10^{10} \text{ Bq}$	$9.5 \times 10^{10} \text{ Bq}$
Total number of $\beta$ electrons	$1.48 \times 10^6$	$3.68 \times 10^6$
$\beta$ -electron-to-background ratio	3.7	9.9

The total  $\beta$ -electron count is given for the analysis interval, extending from  $E_0 - 40 \text{ eV}$  to  $E_0$ . The  $\beta$ -electron-to-background ratio is given by the ratio of this number to the background counts in the same energy range. Table reproduced from Reference 29.

Here,  $A_s$  is a normalization factor and  $N_{T,\text{eff}}$  the effective number of tritium atoms in the source, taking into account the detector efficiency and the acceptance angle of the setup  $\theta_{\text{max}} \approx 50.4^\circ$ .  $\theta_{\text{max}}$  is a pitch angle measured between the  $\beta$  momentum and the local magnetic-field line. The response function  $f(E, qU)$  defines the probability of transmission of an electron with a starting energy of  $E$  through the beamline as a function of the retarding energy  $qU$ . It is dominated by the propagation and scattering of the electrons in the source and by the energy filtering of electrons by the main spectrometer:

$$f(E, qU) = \int_{\epsilon=0}^{E-qU} \int_{\theta=0}^{\theta_{\text{max}}} \mathcal{T}(E - \epsilon, \theta, qU) \sin \theta \sum_s P_s(\theta) f_s(\epsilon) d\theta d\epsilon. \quad 5.$$

$\mathcal{T}(E - \epsilon, \theta, qU)$  is the transmission function of the main spectrometer, which evaluates to either 1 or 0, depending on the starting energy  $E$  and lost energy  $\epsilon$  of the electron, on the pitch angle  $\theta$ , and on three magnetic fields:  $B_{\text{src}}$  at the starting point,  $B_{\text{ana}}$  in the spectrometer's analyzing plane, and  $B_{\text{max}}$  at the magnetic-field maximum. The energy-loss function  $f_1(\epsilon)$  of electrons due to a single scattering interaction in the source was measured separately (Section 2.3). The energy-loss function  $f_s(\epsilon)$  due to  $s$ -fold scattering is obtained by convolution of  $f_1$  with itself and is weighted with the scattering probability  $P_s(\theta)$ , which depends on the path length of electrons in the source and on the column density. The response function  $f(E, qU, r_j)$  for electrons striking a particular region  $r_j$  of the detector may be obtained by replacing the generalized transmission function  $\mathcal{T}(E - \epsilon, \theta, qU)$  with one specific to that region, accounting for inhomogeneities in  $U$  and  $B_{\text{ana}}$ .

The integral spectrum has four free parameters: the neutrino mass squared  $m_\nu^2$ , the endpoint energy  $E_0$ , the signal amplitude  $A_s$ , and the background rate  $R_{\text{bg}}$ . To infer the values of the free parameters, the modeled integral  $\beta$  spectrum  $R(qU)$  is fitted to the measured spectrum constructed as described in Section 3.1. For the set of scanned retarding energies  $q\vec{U}$  and detector regions (e.g., rings)  $\vec{r}$ , a set of measured count rates  $\vec{R}_{\text{data}}(q\vec{U}, \vec{r})$  is obtained, and  $\vec{R}(q\vec{U}, \vec{r}|\vec{\Theta}, \vec{\eta})$  describes the model prediction of these rates. The free parameters  $\vec{\Theta}$  contain a common  $m_\nu^2$  parameter with  $E_0$ ,  $A_s$ , and  $R_{\text{bg}}$  independent for each of the detector regions. The spectrum is also impacted by a set of systematic parameters  $\vec{\eta}$  that are usually determined via independent calibration measurements (see Section 2.3). The fit parameters are inferred by a minimization of the function  $\chi^2 = [\vec{R}_{\text{data}}(q\vec{U}, \vec{r}) - \vec{R}(q\vec{U}, \vec{r}|\vec{\Theta}, \vec{\eta})]^T \cdot C^{-1} \cdot [\vec{R}_{\text{data}}(q\vec{U}, \vec{r}) - \vec{R}(q\vec{U}, \vec{r}|\vec{\Theta}, \vec{\eta})]$ . The covariance matrix  $C$  always includes the statistical uncertainties, and in one analysis approach, it also describes the systematic uncertainties as described below. The uncertainties of the parameters  $\vec{\eta}$  are incorporated into the spectral fits in several different ways (see References 64 and 29 for more details).

In the pull-term method, a parameter  $\eta_i$  is treated as a free fit parameter, but the  $\chi^2$  function acquires an additional term  $\left(\frac{\hat{\eta}_i - \eta_i}{\sigma_{\eta_i}}\right)^2$ , where  $\hat{\eta}_i$  is the estimation of the parameter from an external measurement and  $\sigma_{\eta_i}$  is its uncertainty. This term effectively constrains the parameter while allowing for some variation. The  $\chi^2$  minimization procedure automatically takes into account the correlations between free and constrained parameters.

The covariance-matrix approach incorporates the systematic uncertainties of parameters  $\vec{\eta}$  directly into the covariance matrix. To build  $C$  at a given  $qU_i$  and  $r_j$ , the  $\beta$  spectra  $R_{ijk}(qU_i, r_j | \vec{\Theta}, \vec{\eta})$  are computed  $\mathcal{O}(10^4)$  times, with each systematic parameter  $\eta_k$  varied assuming a normal distribution with the mean at  $\hat{\eta}_k$  and the variance at  $\sigma_{\eta_k}$ . The covariance matrix of the resulting spectral points  $R(qU_i, r_j)$  is estimated from this sample. It can be precalculated for each individual systematic effect and permits very flexible studies of the systematic uncertainties.

The Monte Carlo propagation method addresses systematic uncertainties by multiple [ $\mathcal{O}(10^5)$ ] repetitions of the spectral fit, with systematic parameters  $\eta_k$  being fixed to random values sampled from their probability density functions. In the produced distribution of the free fit parameters  $\vec{\Theta}$ , each entry is weighted with the likelihood of the corresponding fit.

A complementary analysis approach exploits Bayesian inference. Here the parameters of interest  $\vec{\Theta}$  are derived in the form of posterior probability distributions from the likelihood function and the prior probability using Bayes's theorem. The systematic parameters  $\eta_k$  are included in the analysis via informative prior distributions. The posterior distribution is produced by a large-sample Markov chain Monte Carlo.

Several teams perform the analysis by using a shared spectrum model and independent software implementations of the analysis methods described above. To prevent experimenter's bias, the data selection, analysis cuts, model composition, and included systematic effects are fixed before the model is fitted to the experimental data, and the fitting is performed using a modified (blinded) model in which a random Gaussian broadening is applied to the electronic ground state of the molecular final-state distribution. The effective width of the ground state is highly correlated with the  $m_\nu^2$  value, but not with the other fit parameters, so that a randomly chosen value of the width hides the true value of the parameter of interest without otherwise affecting the analysis procedure. The analysis is first applied to a Monte Carlo copy of the data, on which statistical and systematic uncertainties as well as the expected sensitivity are computed. In the next step, the blinded model is fitted to the data by the independent analysis codes and teams. Consistent results between the teams give a green light for unblinding the model and then performing the final fits.

The confidence interval for the neutrino mass is obtained by using the Likhov-Tkachov method (67), which provides a robust upper limit on the neutrino mass in the region where the best-fit estimation of  $\hat{m}_\nu^2$  is negative, while preserving the standard Neyman construction. The Feldman-Cousins (68) result is also presented for comparison. In the Bayesian approach, the credibility interval is derived by integrating the posterior distribution of  $m_\nu^2$  from zero to the upper limit, defined by 90% probability.

### 3.3. Early Neutrino-Mass Results

KATRIN acquires neutrino-mass data in distinct, well-defined campaigns, numbered sequentially with the prefix KNM (which denotes KATRIN neutrino mass). Between campaigns, the collaboration performs necessary maintenance (e.g., tritium, cryo, and spectrometer infrastructures) and implements upgrades. Here, we discuss results of the first two measurement campaigns. **Table 1** summarizes the key operational details for both.

As KATRIN's first neutrino-mass campaign, KNM1 (spring 2019) was both a scientific run and a crucial demonstration of the experiment's capabilities (28, 64). The experiment operated at

a reduced column density to mitigate instabilities caused by radiochemical reactions of tritium at the inner metal surfaces that had previously never been exposed to significant quantities of tritium (69); after this burn-in period and additional tritium gas exposure in the circulation system, much higher column densities became possible. The statistical penalty of this lower activity was partially mitigated by reduced scattering in the source: Fewer  $\beta$  electrons downscattered out of the analysis interval. KNM1's 23 days of running thus corresponded to approximately 9 days at nominal column density.

Of the focal-plane detector's 148 pixels, 31 were excluded from analysis (Section 3.1) due to upstream obstructions of the flux tube or (less commonly) significant electronic noise. After data-quality cuts, 274 scans were selected for the analysis. The data from all pixels were combined, and data from scan steps at the same  $qU$  set point were stacked to produce a single overall spectrum (Section 3.1; **Figure 3c**).

Of the methods described in Section 3.2, the KNM1 data were treated according to the covariance-matrix approach, the Monte Carlo propagation approach, and a simplified Bayesian approach. A complete description of the analysis can be found in Reference 64. Three separate, blinded implementations of the two frequentist approaches yielded results that agreed to within a few percent of the total uncertainty, with a best-fit value of  $m_\nu^2 = -1.0_{-1.1}^{+0.9}$  eV<sup>2</sup>. This was interpreted as a  $1\sigma$  statistical fluctuation into the unphysical negative regime; KATRIN computed a 16% probability of obtaining a best-fit value as negative as this result, given the KNM1 sensitivity. KATRIN therefore applied the Lokhov-Tkachov prescription (67) to derive an upper limit of  $m_\nu < 1.1$  eV (90% CL).

The statistical uncertainty of 0.97 eV<sup>2</sup> dominated the systematic uncertainty of 0.32 eV<sup>2</sup>, which in turn was dominated by the non-Poissonian background contribution.

The Bayesian approach offers an alternative method of handling the unphysical region of negative neutrino mass squared. Applying a flat prior for  $m_\nu^2 \geq 0$  eV<sup>2</sup> and accounting for only the four most significant systematic uncertainties, this approach yielded an upper limit of  $m_\nu < 0.9$  eV (90% credible interval).

As a cross-check, the best-fit endpoint value,  $E_0 = 18,573.7 \pm 0.1$  eV, was found to be consistent with expectation from measured <sup>3</sup>He – T atomic-mass differences, given KATRIN's knowledge of its energy scale (64).

For the second neutrino-mass campaign (KNM2) in autumn 2019, the burn-in phase was complete, and KATRIN was able to operate the source close to its nominal column density. Furthermore, bake-out of the main spectrometer with regeneration of the liquid-nitrogen-cooled baffles reduced the non-Poissonian background due to radon (Section 2.3.2), cutting the overall background rate by 25%. Scan-to-scan fluctuations were reduced by an improvement of the high-voltage reproducibility. The same 117 pixels as in KNM1 were used in the analysis. The data were analyzed variously with pixels grouped into 12 rings, into four wider annuli, and into a single uniform detector; the latter spectrum is shown in **Figure 3**. These groupings allowed a test of the hypothesis that plasma effects induced a radial shift in the effective energy scale; in the end, however, no significant radial dependence was observed.

A new blinding factor was applied to the model for KNM2 and was automatically propagated to the various analysis codes. The analysis is described in detail in Reference 29. Briefly, the pull-term method was added to the approaches used for KNM1, and the Bayesian approach was extended to implement additional systematic uncertainties.

All approaches find a slightly positive best-fit value of  $m_\nu^2 = 0.26_{-0.34}^{+0.34}$  eV<sup>2</sup>, consistent with each other within approximately 5% of the total uncertainty. **Table 2** gives the final uncertainty breakdown. The best-fit endpoint value,  $E_0 = 18,573.69 \pm 0.03$  eV, again agrees with expectations. As expected for a positive best-fit value, both the Lokhov-Tkachov and Feldman-Cousins

**Table 2** Comparison of breakdown of larger uncertainties for the neutrino-mass-squared best fits for the first [KNM1 (64)] and second [KNM2 (29)] KATRIN neutrino-mass campaigns

Effect ( $1\sigma$ uncertainty on $m_\nu^2$ )	KNM1 ( $\text{eV}^2$ )	KNM2 ( $\text{eV}^2$ )
Statistical	0.97	0.29
Non-Poissonian background	0.30	0.11
Source-potential variations (plasma effects)	Neglected	0.09
Scan-step-duration-dependent background	Neglected	0.07
$qU$ -dependent background	0.07	0.06
Magnetic fields	0.05	0.04
Molecular final-state distribution	0.02	0.02
Column density $\times$ inelastic scattering cross section ( $\rho d\sigma$ )	0.05	0.01
<b>Total uncertainty</b>	<b>1.02</b>	<b>0.34</b>

The full tabulation is found in References 29 and 64.

prescriptions yield the same upper limit,  $m_\nu < 0.9$  eV (90% CL). At 90% credibility, the corresponding Bayesian limit (with a positive flat prior on  $m_\nu^2$ ) is  $m_\nu < 0.85$  eV.

Since the KATRIN operational parameters differed so significantly between KNM1 and KNM2 (Table 1), it is not possible to describe both campaigns with a single model spectrum. However, as described in Reference 29, several approaches are available to combine the data sets. Figure 3 shows the results of a joint fit between the two data sets, in which the data from all pixels have been combined into a uniform spectrum for each campaign. In this analysis,  $m_\nu^2$  is a shared fit parameter for both campaigns, whereas the parameters  $A_s$ ,  $R_{bg}$ , and  $E_0$  are allowed to differ between KNM1 and KNM2. Pull terms are used to account for the systematic uncertainties, some of which vary between measurement periods and some of which are fit in common. The combined best-fit value of  $m_\nu^2 = 0.07 \pm 0.32$   $\text{eV}^2$  leads to an upper limit of  $m_\nu < 0.75$  eV (90% CL). Figure 4 shows another approach, in which the results of the two measurement campaigns are combined by adding their respective  $\chi^2$  curves. The resulting upper limit is  $m_\nu < 0.81$  eV (90% CL). In a

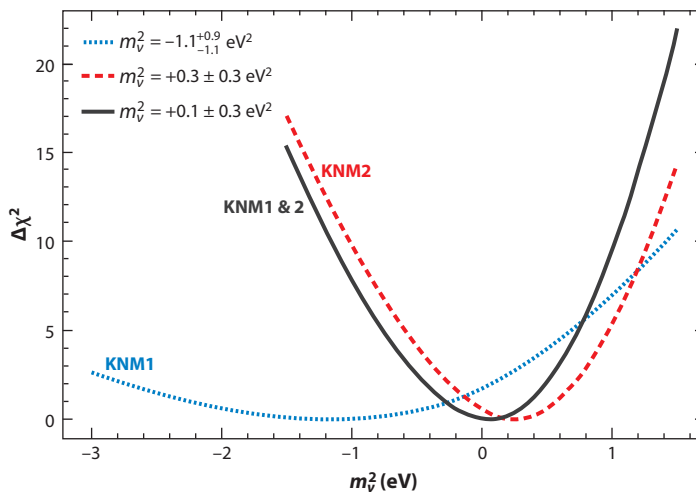


**Figure 4**

$\chi^2$  profiles for the first (KNM1) and second (KNM2) KATRIN neutrino-mass campaigns and the sum of the two for the combined data set.

Bayesian framework, the KNM1 posterior distribution can simply be used as prior information for the KNM2 analysis, neglecting correlations between the two spectra. This procedure results in a Bayesian limit of  $m_\nu < 0.73$  eV (90% credible interval).

These analyses combine all the neutrino-mass data acquired in 2019, but the experiment continued to run throughout 2020 and 2021, with only minor delays due to the COVID-19 pandemic. Section 4 below outlines the technical improvements that were implemented for these later campaigns.

### 3.4. Sterile-Neutrino Results

Beyond a direct neutrino-mass measurement, high-precision  $\beta$  spectroscopy close to the endpoint enables a search for light sterile neutrinos. The electron-flavor neutrino, emitted in a  $\beta$  decay, may contain a small admixture of a hypothetical fourth neutrino-mass eigenstate  $m_4$ . In this case, the  $\beta$ -decay spectrum

$$R_\beta(E) = \cos^2 \Theta_s R_\beta(E, m_\nu^2) + \sin^2 \Theta_s R_\beta(E, m_4^2) \quad 6.$$

would be composed of both the spectrum corresponding to the effective light neutrino mass  $m_\nu^2$  and a spectrum associated with  $m_4$ , in which the maximal energy is reduced to  $E_0 - m_4$ . The amplitudes of the two decay branches are given by  $\cos^2 \Theta_s$  and  $\sin^2 \Theta_s$ , where  $\Theta_s$  is the active-to-sterile mixing angle. The resulting signature of a sterile neutrino is thus a kink-like distortion of the measured spectrum at an energy of  $E_0 - m_4$ .

The existence of light sterile neutrinos is motivated mainly by a number of long-standing anomalies in short-baseline neutrino-oscillation experiments (70, 71). For example, the so-called reactor-antineutrino anomaly (RAA) (72) is a  $2\sigma$  to  $3\sigma$  deficit of the neutrino flux at a distance of 10 to 100 m from a fission reactor, compared to the theoretical expectation. The deficit could be explained by the existence of sterile neutrinos with a mass in the eV range and mixing amplitudes of a few percent. Recent results of STEREO (73), PROSPECT (74), and DANSS (75) exclude the existence of sterile neutrinos in a large part of the preferred parameter space of the RAA but cannot probe squared mass differences above  $\Delta m_{14}^2 = 10$  eV<sup>2</sup>. Interestingly, the BEST experiment reports a new measurement that is consistent with the existence of sterile neutrinos with  $\Delta m_{14}^2 = (m_1^2 - m_4^2)^2 > 10$  eV<sup>2</sup> (76).

KATRIN measures the tritium  $\beta$ -decay spectrum down to approximately 90 eV below the endpoint, allowing for the search for sterile neutrinos up to approximately this mass. The systematic uncertainty evaluation of KATRIN is initially optimized only for an analysis window of 40 eV below  $E_0$ , and we restrict the sterile-neutrino search accordingly. As the statistics of the  $\beta$ -decay spectrum increase further away from the endpoint, the statistical sensitivity increases for a sterile neutrino with larger mass. This feature makes the search with KATRIN complementary to oscillation-based searches, which are often limited in resolving the high-frequency oscillatory signature of heavy sterile neutrinos. Due to limited position resolution or extended source dimensions, oscillation-based experiments would observe the signature of sterile neutrinos above a certain mass only as an overall rate reduction.

The KATRIN collaboration performed a sterile-neutrino search based on the first two physics runs (Section 3.3). The analysis is performed by computing  $\chi^2$  in a manner similar to that described in Section 3.2, but with a spectrum model according to Equation 6. At each point on a  $(m_4, \sin^2 \Theta_s)$  grid,  $\Delta\chi^2 = \chi^2 - \chi_{\text{best}}^2$  is computed, where  $\chi_{\text{best}}^2$  corresponds to the global best fit in the grid. According to Wilks's theorem (77), we exclude  $m_4$  and  $\sin^2 \Theta_s$  values for which  $\Delta\chi^2 > 4.6$  at 90% CL. The applicability of Wilks's theorem was tested on extensive Monte Carlo simulations.

For comparison with oscillation experiments, the exclusion limits are transformed to the  $[\Delta m_{14}^2, \sin^2(2\Theta_{14})]$  plane under the assumption that  $m_1$  is zero. The result is displayed in **Figure 5**. For

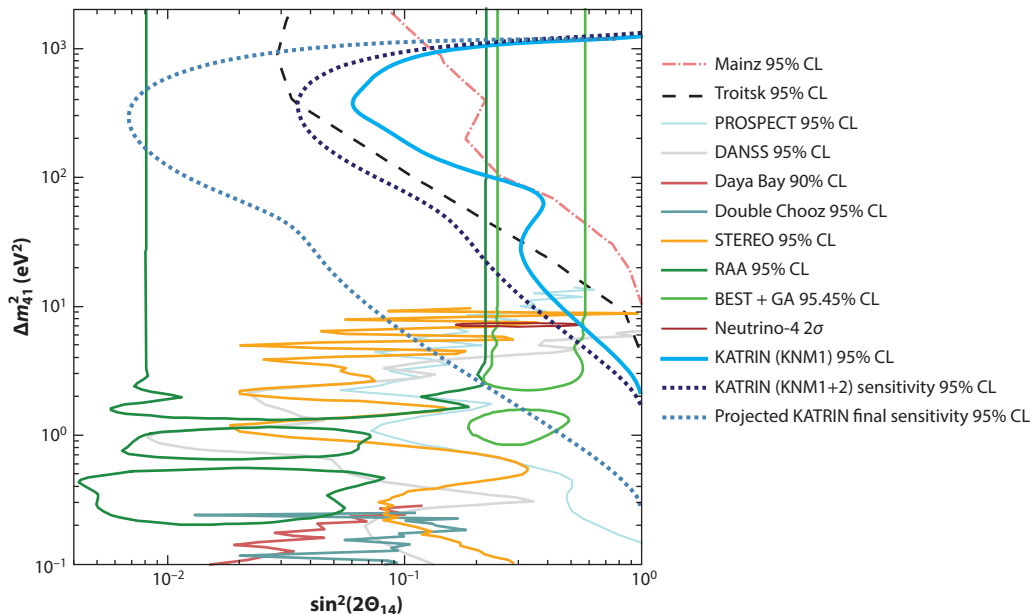


**Figure 5**

Precision measurements of the tritium  $\beta$ -decay spectrum can probe for a mixing contribution of light sterile neutrinos. Here, we show the exclusion bounds on the mass-square splitting  $\Delta m_{41}^2$  and the mixing angle  $\sin^2(2\Theta_{14})$  obtained with direct kinematics measurements in the Mainz and Troitsk experiments, as well as with the first science run of KATRIN (KNM1). Also shown is the expected sensitivity for the first two KATRIN campaigns combined (KNM1+2) and the projected sensitivity after 1,000 full measurement days. Overlaid are the parameter constraints from several oscillation experiments. See Reference 80 for details.

both measurement campaigns, KATRIN finds a best fit that is consistent with the null hypothesis, and it thus sets an upper limit on the sterile-neutrino parameters. A combined fit of the first two KATRIN data sets improves the limits relative to the Mainz and Troitsk experiments. Above  $\Delta m_{41}^2 = 10 \text{ eV}^2$ , KATRIN improves limits with respect to oscillation-based searches and starts testing the best-fit regions of BEST (combined with the gallium anomaly) and the RAA. With the final KATRIN data set, large parts of the parameter space consistent with the BEST result and the Neutrino-4 (78) hint will be probed.

References 79 and 80 give a detailed description of the KATRIN sterile-neutrino analysis, including discussion of the degeneracy of the neutrino-mass and sterile-neutrino signatures.

## 4. THE FUTURE OF KATRIN

### 4.1. Outlook on Long-Term Data Taking and Projected Sensitivity

The present upper limits on the neutrino mass (Section 3) are obtained with 2019 data only—effectively 40 out of a planned 1,000 measurement days. Four additional neutrino-mass campaigns, with a total time of 250 days, were completed in 2020 and 2021. The integrated acquired data are shown in **Figure 6**. Starting in 2020, several upgrades and extended calibrations improved the background rate and systematic uncertainties.

A new background-reduction technique, termed the shifted analyzing plane, is based on the strong dependence of the main component of the background rate on the volume of the main spectrometer that is imaged by the detector (Section 2.3.2). Reducing the volume by fine-tuning the electromagnetic fields in the spectrometer leads to a twofold background-rate decrease. This

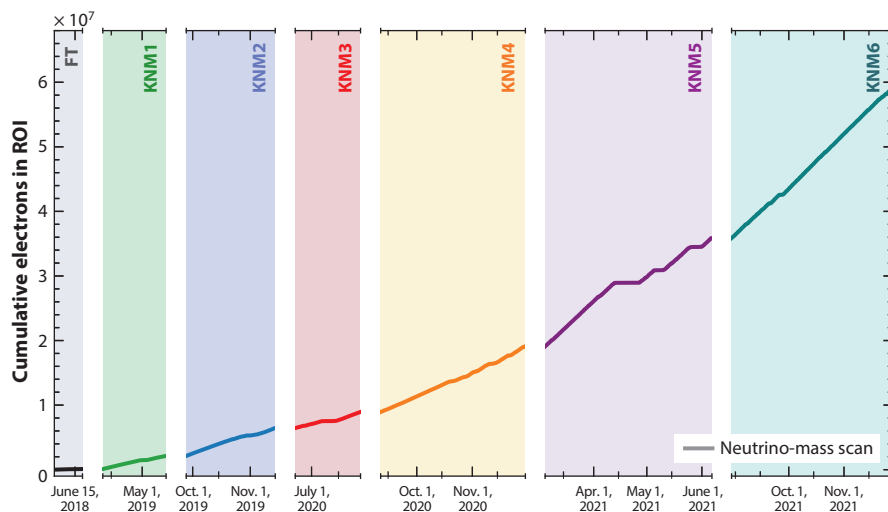


**Figure 6**

Overview of  $\beta$ -spectrum measurements acquired since the first tritium (FT) campaign in the commissioning phase of 2018. Accumulated electron counts are shown in the neutrino-mass region of interest (ROI; extending to 40 eV below the spectral endpoint  $E_0$ ) over six measurement phases (KNM1–6).

measurement mode was implemented in the third neutrino-mass measurement campaign (June–July 2020) after dedicated calibration measurements of the magnetic field and electric potential and tritium test scans (81).

Another modification deals with tritium-source-related effects and uncertainties described in Section 2.3.1. An in situ measurement of the starting potential is done by injecting gaseous  $^{83m}\text{Kr}$  into the source, along with tritium, and scanning the narrow conversion-electron lines. The conditions of this calibration measurement should be as close as possible to those of the neutrino-mass scans. For that reason, the nominal temperature of the source has been increased to 80 K (compared to 30 K in the original design), preventing freezing of krypton gas. The column density of tritium in the source is limited to 75% of the original nominal value by the higher conductance at elevated source temperature. The tritium gas circulation was modified: The full tritium flow is not filtered by a palladium-silver membrane but partially bypasses this hydrogen-isotope-selective component. In this mode, the high tritium purity is preserved, and an admixture of  $^{83m}\text{Kr}$  can be cocirculated under these beta-scan conditions (82). However, the amount of krypton is reduced by at least two orders of magnitude. To compensate for the loss of statistics, a stronger source and longer measurement time are required. A 10-GBq  $^{83m}\text{Kr}$  source produced in Řež (83) was used in 2021 to derive the source-potential variation with a precision better than 10 meV.

Along with these two major modifications, at the beginning of 2021 ozone was used to remove accumulated tritium from the rear wall of the source. This process mitigated the impact of residual tritium on the measured spectrum and therefore on the neutrino-mass analysis. The uncertainties of the source magnetic field and  $qU$ -dependent background have been reduced through precise calibration measurements. New computations of the molecular final states are expected to significantly improve the corresponding uncertainty.

The data accumulated through summer 2021 take the KATRIN neutrino-mass sensitivity to the level of 0.5 eV (90% CL). Even after the implementation of the shifted-analyzing-plane

configuration, however, the background rate still exceeds the design requirement by a factor of 10. The statistical sensitivity to the neutrino mass is thereby degraded by a factor of 1.5. Several promising projects target further reduction of the background rate to reach the sensitivity goal of 0.2 eV (90% CL). First, one can exploit a specific angular distribution of the background electrons and discriminate against background through angular-selective detection of electrons. Second, deexcitation of the progenitor Rydberg atoms using terahertz radiation can actively restrict creation of background electrons. Time-of-flight tagging methods are also under investigation but are technically very challenging. If proven successful, such measures should be implemented as early as possible to gain the most from the background reduction.

## 4.2. Beyond-Standard-Model Physics in Precision $\beta$ -Decay Spectroscopy

High-precision  $\beta$  spectroscopy has a rich physics program beyond the determination of the neutrino mass. The scientific reach can be further enlarged by extending the measurement interval from a region close to the endpoint to a region covering the full tritium  $\beta$ -decay spectrum or a large fraction of it. A high-statistics measurement of the entire tritium  $\beta$ -decay spectrum by KATRIN after an exchange of the current focal-plane detector with the TRISTAN detector (84) is currently being investigated (see Section 4.2.3).

**4.2.1. Relic-neutrino search.** One second after the Big Bang, neutrinos froze out of thermal equilibrium with matter and have been free streaming since then. Today the universe is filled with approximately 336 relic cosmic neutrinos per  $\text{cm}^3$ . Their temperature of 1.9 K, corresponding to meV energies, makes their direct detection very challenging and so far unrealized.

Relic neutrinos can be captured by tritium (85). Since tritium is not stable, this reaction has no energy threshold. Electrons emitted in the subsequent decay will have energies of  $E = E_0 + m_\nu$ , leading to a peak feature above the endpoint. If one assumed an average density of relic neutrinos in the universe, the capture rate on 100 g of tritium would yield a handful of events per year (86). However, some cosmological models predict large (up to  $10^6 \times$ ) overdensities of relic neutrinos in the center of our galaxy (87–89).

The source beam tube of the KATRIN experiment contains approximately 30  $\mu\text{g}$  of gaseous tritium at any given time. KATRIN performed a first search for relic neutrinos on the basis of the initial two measurement campaigns (90). The search revealed no signal of relic neutrinos and constrained the overdensity factor to  $\eta < 10^{11}$ , the most stringent bound obtained in a direct experiment so far. With the full KATRIN statistics and the current background level, a sensitivity of  $\eta < 10^{10}$  is expected.

**4.2.2. Lorentz-invariance violation.** Some theories beyond the Standard Model predict deviations from Lorentz invariance (LI). Violations of Lorentz symmetry are typically described by a certain parametrization in effective theories. Many of the LI-violating parameters are strongly constrained by time-of-flight or neutrino-oscillation experiments. However, some parameters have no constraints or have only very weak ones (91–93).

The three-dimensional oscillation-free parameter  $a_{\text{of}}$  would introduce a preferred direction in space, manifesting in an anisotropic  $\beta$ -decaying source as a sidereal oscillation of the spectral endpoint  $E_0$  (92, 94). As KATRIN analyzes only electrons that are emitted with an angle smaller than  $50.4^\circ$  relative to the beam axis, it can be sensitive to this parameter.

KATRIN performed a search for LI violation on the basis of its first science run. This campaign featured approximately 300  $\beta$  scans over a time period of 2 weeks. For each scan, KATRIN inferred the effective endpoint and, from these endpoints, found the best-fit oscillatory signature with the

required period of 23.7 h. This analysis finds no sign of LI violation, thus setting the first limit on  $a_{\text{of}}$  (95).

**4.2.3. Sterile-neutrino search.** As described in Section 3.4, KATRIN is sensitive to light sterile neutrinos, providing information complementary to oscillation-based searches. As the analysis interval of KATRIN is currently constrained to 40 eV below  $E_0$ , only sterile neutrinos up to a corresponding mass of approximately  $m_4 < 40$  eV can be searched for.

To search for heavier sterile neutrinos, a larger range of the tritium  $\beta$  spectrum must be measured. In particular, keV-scale sterile neutrinos are potential dark-matter candidates (96). However, indirect observations and cosmological considerations limit their mixing with active neutrinos to  $\sin^2 \Theta_s < 10^{-6}$ .

As the count rate increases further away from the endpoint, the statistical uncertainty decreases. A yearlong measurement at the KATRIN source strength would yield a statistical sensitivity at the level of  $\sin^2 \Theta_s < 10^{-6}$  (97, 98). However, a high-statistics measurement of the entire tritium  $\beta$ -decay spectrum poses a new technical challenge: electron rates exceeding  $10^8$  cps. Moreover, new systematic uncertainties become relevant when one is describing the experimental tritium spectrum far away from the endpoint.

The TRISTAN project is exploring the sensitivity of such a search and is developing a new silicon drift detector focal-plane array for KATRIN with more than 1,000 pixels (84, 99). This technology allows for measurement of a high  $\beta$ -electron flux with large pixel footprints and an energy resolution of 300 eV for 20-keV electrons, enabling a differential measurement of the full tritium  $\beta$ -decay spectrum. The new detector will be installed after completion of the neutrino-mass measurements.

**4.2.4. Other beyond-Standard-Model signals.** An ultraprecise measurement of the tritium  $\beta$ -decay spectrum would also allow for searches for other phenomena beyond the Standard Model, including the emission of new light bosons (100), exotic charged-current interactions (101), extradimensional sterile neutrinos (102), right-handed currents (103), and neutrino interactions with a dark field (104). Further searches may be contemplated as theory advances.

## 5. SUMMARY

The  $\beta$ -decay kinematics of tritium have been exploited to probe the neutrino-mass scale since before the first experimental observation of neutrinos. As shown in **Figure 7**, the upper limit has improved by more than three orders of magnitude throughout seven decades of progress in experimental techniques, analysis methods, and theoretical calculations. The KATRIN experiment, which has operated since spring 2019, is the practical culmination of the powerful MAC-E-filter technique (Section 2). KATRIN has pushed the upper limit down to  $m_\nu < 0.8$  eV (90% CL) (29) (Section 3.3) on the sole basis of its first several weeks of data taking. Further experimental improvements address both backgrounds and systematic uncertainties (Section 4) to approach the target sensitivity of 0.2 eV. In addition to being sensitive to the neutrino-mass scale, KATRIN's precise spectral measurements are sensitive to sterile neutrinos (Section 3.4) and other beyond-Standard-Model phenomena (Section 4.2). Meanwhile, other collaborations are exploring alternate tritium measurement techniques and probes with neutrino-emitting, electron-capture-decay isotopes. As a direct kinematic investigation of the neutrino-mass scale, KATRIN's ultimate result will serve as a test of cosmology, a guide to possible neutrinoless-double-beta-decay rates, and an input to particle theory. Its searches for sterile neutrinos, Lorentz-invariance violation, and relic neutrinos will probe new regions of parameter space. After 20 years, KATRIN's story has just begun.

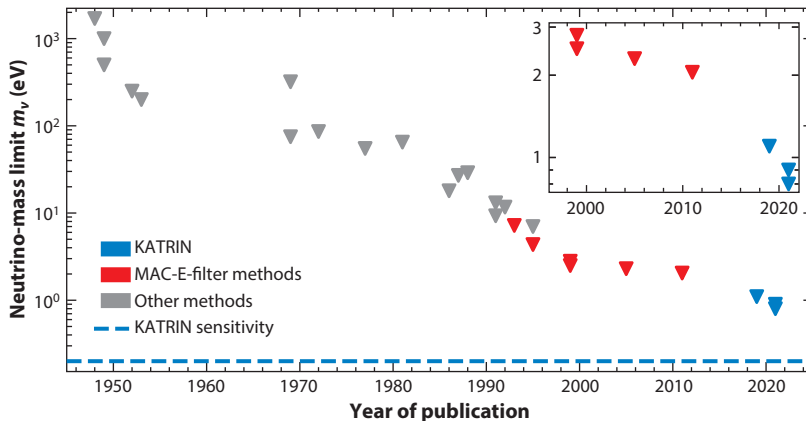


**Figure 7**

Evolution of the upper limit of the neutrino mass over a period of 72 years, based on tritium  $\beta$ -decay experiments. The data selection is according to References 3 and 11. The inset zooms in on the most recent results from Mainz (17), Troitsk (18), and KATRIN (28, 29).

## DISCLOSURE STATEMENT

The authors are funded members of the KATRIN collaboration. They are not aware of any other affiliations, memberships, funding, or financial holdings that might be perceived as affecting the objectivity of this review.

## ACKNOWLEDGMENTS

The authors wish to thank Leonard Köllenberger for his detailed work on many of the figures included in this article. The authors gratefully acknowledge the support of their work: A.L. through the German Federal Ministry for Education and Research (BMBF) (05A20PMA); D.S.P. under US Department of Energy (DOE) award DE-SC0019304; S.M. through BMBF (05A17WO3), the Max Planck Research Group (MaxPlanck@TUM program), the Deutsche Forschungsgemeinschaft (DFG) Sonderforschungsbereich (SFB-1258), and the European Research Council under the European Union Horizon 2020 research and innovation program (grant agreement 852845); and K.V. through the Initiative and Networking Fund of the Helmholtz Association (grant numbers W2/W3-118 and VH-NG-1055). The KATRIN collaboration is additionally supported by the Helmholtz Association, BMBF (5A17PDA, 05A17PM3, 05A17PX3, and 05A17VK2), the Helmholtz Alliance for Astroparticle Physics, and DFG (Research Training Groups GRK 1694 and GRK 2149 and Graduate School GSC 1085-KSETA) in Germany; the Ministry of Education, Youth, and Sport (CANAM-LM2011019, LTT19005) in the Czech Republic; and the US DOE through grants DE-FG02-97ER41020, DE-FG02-94ER40818, DE-SC0004036, DE-FG02-97ER41033, DE-FG02-97ER41041, DE-AC02-05CH11231, and DE-SC0011091 and the National Energy Research Scientific Computing Center.

## LITERATURE CITED

1. Fukuda Y, et al. *Phys. Rev. Lett.* 81:1562 (1998)
2. Ahmad QR, et al. *Phys. Rev. Lett.* 89:011301 (2002)
3. Formaggio JA, de Gouvêa ALC, Robertson RGH. *Phys. Rep.* 914:1 (2021)
4. Abbott TMC, et al. *Phys. Rev. D* 105:023520 (2022)

5. Loredo TJ, Lamb DQ. *Phys. Rev. D* 65:063002 (2002)
6. Dolinski MJ, Poon AWP, Rodejohann W. *Annu. Rev. Nucl. Part. Sci.* 69:219 (2019)
7. Agostini M, et al. *Phys. Rev. Lett.* 125:252502 (2020)
8. Gando A, et al. *Phys. Rev. Lett.* 117:082503 (2016)
9. Bodine LI, Parno DS, Robertson RGH. *Phys. Rev. C* 91:035505 (2015)
10. Braß M, Haverkort MW. *New J. Phys.* 22:093018 (2020)
11. Zyla PA, et al. *PTEP* 2020:083C01 (2020)
12. Saenz A, Jonsell S, Froelich P. *Phys. Rev. Lett.* 84:242 (2000)
13. Otten EW, Weinheimer C. *Rep. Prog. Phys.* 71:086201 (2008)
14. Picard A, et al. *Nucl. Instrum. Methods B* 63:345 (1992)
15. Lobashev VM, Spivak PE. *Nucl. Instrum. Methods A* 240:305 (1985)
16. Wilkerson JF, et al. *Phys. Rev. Lett.* 58:2023 (1987)
17. Kraus C, et al. *Eur. Phys. J. C* 40:447 (2005)
18. Aseev VN, et al. *Phys. Rev. D* 84:112003 (2011)
19. Monreal B, Formaggio JA. *Phys. Rev. D* 80:051301 (2009)
20. Ashtari Esfahani A, et al. *J. Phys. G* 44:054004 (2017)
21. De Rujula A, Lusignoli M. *Phys. Lett. B* 118:429 (1982)
22. Gastaldo L, et al. *Eur. Phys. J. Spec. Top.* 226:1623 (2017)
23. Fleischmann A, Enss C, Seidel G. In *Cryogenic Particle Detection*, pp. 151–216. Berlin/Heidelberg: Springer (2005)
24. Gastaldo L, et al. *AIP Conf. Proc.* 1185:607 (2009)
25. Alpert B, et al. *Eur. Phys. J. C* 75:112 (2015)
26. Puiu A, et al. *J. Low Temp. Phys.* 199:716 (2020)
27. Velte C, et al. *Eur. Phys. J. C* 79:1026 (2019)
28. Aker M, et al. *Phys. Rev. Lett.* 123:221802 (2019)
29. Aker M, et al. *Nat. Phys.* 18:160 (2022)
30. Osipowicz A, et al. arXiv:hep-ex/0109033 (2001)
31. Aker M, et al. *J. Instrum.* 16:T08015 (2021)
32. Aker M, et al. *Sensors* 20:4827 (2020)
33. Röllig M, et al. *Fusion Eng. Des.* 100:177 (2015)
34. Beglarian A, et al. *J. Instrum.* 17:T03002 (2022)
35. Vénos D, et al. *J. Instrum.* 9:P12010 (2014)
36. Bornschein B, et al. *Fusion Sci. Tech.* 71:231 (2017)
37. Arenz M, et al. *J. Instrum.* 11:P04011 (2016)
38. Wandkowsky N, et al. *J. Phys. G* 40:085102 (2013)
39. Fraenkle FM. *J. Phys. Conf. Ser.* 888:012070 (2017)
40. Altenmüller K, et al. *Astropart. Phys.* 108:40 (2019)
41. Altenmüller K, et al. *Eur. Phys. J. C* 79:807 (2019)
42. Behrens JD. 2016. *Design and commissioning of a mono-energetic photoelectron source and active background reduction by magnetic pulse at the KATRIN spectrometers*. PhD Thesis, Westfälische Wilhelms-Universität Münster
43. Babutzka M, et al. *New J. Phys.* 14:103046 (2012)
44. Grohmann S, Bode T, Schön H, Süßner M. *Cryogenics* 51:438 (2011)
45. Grohmann S, et al. *Cryogenics* 55–56:5 (2013)
46. Arenz M, et al. *J. Instrum.* 13:P04020 (2018)
47. Altenmüller K, et al. *J. Phys. G* 47:065002 (2020)
48. Arenz M, et al. *Eur. Phys. J. C* 78:368 (2018)
49. Rest O, et al. *Metrologia* 56:045007 (2019)
50. Aker M, et al. *Eur. Phys. J. C* 80:264 (2020)
51. Röttele C. 2019. *Tritium suppression factor of the KATRIN transport section*. PhD Thesis, Karlsruhe Institute of Technology
52. Klein M. 2018. *Tritium ions in KATRIN: blocking, removal and detection*. PhD Thesis, Karlsruhe Institute of Technology

53. Schlösser M, et al. *Fusion Sci. Tech.* 76:170 (2020)
54. Friedel FR. 2020. *Ion and plasma systematics during the first KATRIN neutrino mass measurements*. PhD Thesis, Karlsruhe Institute of Technology
55. Vizcaya Hernández AP. 2021. *Toward a measurement of the neutrino mass with tritium: ion studies for the KATRIN and TRIMS experiments*. PhD Thesis, Carnegie Mellon University
56. Aker M, et al. *Eur. Phys. J. C* 81:579 (2021)
57. Letnev J, et al. *J. Instrum.* 13:T08010 (2018)
58. Furse D, et al. *New J. Phys.* 19:053012 (2017)
59. Arenz M, et al. *J. Instrum.* 13:T08005 (2018)
60. Angrik J, et al. (KATRIN Collab.) 2005. *KATRIN design report 2004*. Rep., KATRIN Collab. <https://doi.org/10.5445/IR/270060419>
61. Harms F. 2015. *Characterization and minimization of background processes in the KATRIN main spectrometer*. PhD Thesis, Karlsruhe Institute of Technology
62. Fränkle F, et al. *Astropart. Phys.* 138:102686 (2022)
63. Aker M, et al. *Eur. Phys. J. C* 80:821 (2020)
64. Aker M, et al. *Phys. Rev. D* 104:012005 (2021)
65. Amsbaugh JF, et al. *Nucl. Instrum. Methods A* 778:40 (2015)
66. Kleesiek M, et al. *Eur. Phys. J. C* 79:204 (2019)
67. Lokhov AV, Tkachov FV. *Phys. Part. Nucl.* 46:347 (2015)
68. Feldman GJ, Cousins RD. *Phys. Rev. D* 57:3873 (1998)
69. Sturm M, et al. *Fusion Eng. Des.* 170:112507 (2021)
70. Abazajian KN, et al. arXiv:1204.5379 [hep-ph] (2012)
71. Giunti C, Lasserre T. *Annu. Rev. Nucl. Part. Sci.* 69:163 (2019)
72. Mention G, et al. *Phys. Rev. D* 83:073006 (2011)
73. Almazán H, et al. *Phys. Rev. D* 102:052002 (2020)
74. Andriamirado M, et al. *Phys. Rev. D* 103:032001 (2021)
75. Danilov M. *Proc. Sci. EPS-HEP2019*:401 (2020)
76. Barinov VV, et al. arXiv:2109.11482 [hep-ph] (2021)
77. Wilks SS. *Ann. Math. Stat.* 9:60 (1938)
78. Serebrov AP, et al. *Phys. Rev. D* 104:032003 (2021)
79. Aker M, et al. *Phys. Rev. Lett.* 126:091803 (2021)
80. Aker M, et al. *Phys. Rev. D* 105:072004 (2022)
81. Lokhov A, et al. *Eur. J. Phys. C* 82:258 (2022)
82. Aker M, et al. *Operation modes of the KATRIN experiment tritium loop system using  $^{83m}\text{Kr}$* . Work. Pap., KATRIN Collab. (2022)
83. Sentkerestiová J, et al. *J. Instrum.* 13:P04018 (2018)
84. Mertens S, et al. *J. Phys. G* 46:065203 (2019)
85. Cocco AG, Mangano G, Messina M. *J. Cosmol. Astropart. Phys.* 0706:015 (2007)
86. Long AJ, Lunardini C, Sabancilar E. *J. Cosmol. Astropart. Phys.* 1408:038 (2014)
87. Ringwald A. arXiv:hep-ph/0505024 (2005)
88. Hodak R, et al. arXiv:1102.1799 [hep-ph] (2011)
89. de Salas P, Gariazzo S, Lesgourgues J, Pastor S. *J. Cosmol. Astropart. Phys.* 1709:034 (2017)
90. Aker M, et al. arXiv:2202.04587 [nucl-ex] (2022)
91. Díaz JS, Kostelecký VA, Lehnert R. *Phys. Rev. D* 88:071902 (2013)
92. Kostelecký VA, Mewes M. *Phys. Rev. D* 85:096005 (2012)
93. Lehnert R. *Hyperfine Interact.* 193:275 (2009)
94. Lehnert R. arXiv:2112.13803 [hep-ph] (2021)
95. Aker M, et al. *Search for Lorentz violation with the first KATRIN data*. Work. Pap., KATRIN Collab. (2022)
96. Drewes M, et al. *J. Cosmol. Astropart. Phys.* 1701:025 (2017)
97. Mertens S, et al. *J. Cosmol. Astropart. Phys.* 1502:020 (2015)
98. Mertens S, et al. *Phys. Rev. D* 91:042005 (2015)

99. Mertens S, et al. *J. Phys. G* 48:015008 (2020)
100. Arcadi G, et al. *J. High Energy Phys.* 1901:206 (2019)
101. Ludl PO, Rodejohann W. *J. High Energy Phys.* 1606:40 (2016)
102. Rodejohann W, Zhang H. *Phys. Lett. B* 737:81 (2014)
103. Barry J, Heeck J, Rodejohann W. *J. High Energy Phys.* 1407:81 (2014)
104. Huang G, Rodejohann W. arXiv:2110.03718 [hep-ph] (2021)

# Contents

The Road to Precision Cosmology <i>Michael S. Turner</i> .....	1
<i>B</i> Flavor Anomalies: 2021 Theoretical Status Report <i>David London and Joaquim Matias</i> .....	37
Testing Lepton Flavor Universality with Pion, Kaon, Tau, and Beta Decays <i>Douglas Bryman, Vincenzo Cirigliano, Andreas Crivellin, and Gianluca Inguglia</i> .....	69
Something Can Come of Nothing: Surface Approaches to Quantum Fluctuations and the Casimir Force <i>Giuseppe Bimonte, Thorsten Emig, Noah Graham, and Mebran Kardar</i> .....	93
Exotic Higgs Decays <i>María Cepeda, Stefania Gori, Verena Ingrid Martinez Outschoorn, and Jessie Shelton</i> .....	119
Fundamental Neutron Physics at Spallation Sources <i>Nadia Fomin, Jason Fry, Robert W. Pattie Jr., and Geoffrey L. Greene</i> .....	151
Exploring Stars in Underground Laboratories: Challenges and Solutions <i>Marialuisa Aliotta, Axel Boeltzig, Rosanna Depalo, and György Gyürky</i> .....	177
Status of Lattice QCD Determination of Nucleon Form Factors and Their Relevance for the Few-GeV Neutrino Program <i>Aaron S. Meyer, André Walker-Loud, and Callum Wilkinson</i> .....	205
Precision QCD Physics at the LHC <i>Thomas Gebrmann and Bogdan Malaescu</i> .....	233
Probing the Neutrino-Mass Scale with the KATRIN Experiment <i>Alexey Lokhov, Susanne Mertens, Diana S. Parno, Magnus Schlösser, and Kathrin Valerius</i> .....	259
Electroweak Penguin Decays of <i>b</i> -Flavored Hadrons <i>Ulrik Egede, Shobei Nishida, Mitesh Patel, and Marie-Hélène Schune</i> .....	283
Progress in Understanding Short-Range Structure in Nuclei: An Experimental Perspective <i>John Arrington, Nadia Fomin, and Axel Schmidt</i> .....	307

Short-Lived Nuclides in the Early Solar System: Abundances, Origins, and Applications <i>Andrew M. Davis</i> .....	339
High-Energy Extragalactic Neutrino Astrophysics <i>Naoko Kurahashi, Kohta Murase, and Marcos Santander</i> .....	365
The Proton Structure in and out of Muonic Hydrogen <i>Aldo Antognini, Franziska Hagelstein, and Vladimir Pascalutsa</i> .....	389
Novel Quantum Sensors for Light Dark Matter and Neutrino Detection <i>Sunil R. Golwala and Enectali Figueroa-Feliciano</i> .....	419
Searches for Heavy Resonances with Substructure <i>Petar Maksimović</i> .....	447

## Errata

An online log of corrections to *Annual Review of Nuclear and Particle Science* articles may be found at <http://www.annualreviews.org/errata/nucl>